Signal-Flow-Based Analysis and Design of Pseudo-Doherty Load-Modulated Balanced Amplifier Toward Unlimited RF Bandwidth

Pingzhu Gong[®], Student Member, IEEE, Jiachen Guo, Student Member, IEEE, Niteesh Bharadwaj Vangipurapu[®], Graduate Student Member, IEEE, and Kenle Chen[®], Senior Member, IEEE

Abstract—This article reports a first-ever decade-bandwidth pseudo-Doherty load-modulated balanced amplifier (PD-LMBA), designed for emerging 4G/5G communications and multiband operations. By revisiting the load-modulated balanced amplifier (LMBA) theory using an S-matrix-based signal-flow approach, a generalized theory for wideband LMBA operation is developed, taking into account the frequency-dependent nature of all components. In addition, by analyzing the signal-flow behavior of LMBA, a frequency-agnostic phase-alignment condition is identified as critical for ensuring intrinsic broadband load modulation. This unique design methodology enables, for the first time, the independent optimization of broadband balanced amplifier (BA, as the peaking) and control amplifier (CA, as the carrier), thus fundamentally addressing the longstanding limits imposed on the design of wideband load-modulated power amplifiers (PAs). To prove the proposed concept, an ultrawideband RFinput PD-LMBA is designed and developed using GaN technology covering the frequency range from 0.2 to 2 GHz. Experimental results demonstrate an efficiency of 51%-72% for peak output power and 44%-62% for 10-dB output power back-off (OBO), respectively.

Index Terms—Balanced amplifier (BA), de-embedding, Doherty, high efficiency, load modulation, parasitic, phase alignment, power amplifier (PA), signal-flow graph, wideband.

I. INTRODUCTION

In MODERN wireless communication systems, the demand for higher data rates is continuously growing. To transmit high-data-rate signals within limited spectrum resources, sophisticated modulation schemes such as high-order quadrature amplitude modulation (e.g., 1024QAM) and orthogonal frequency-division multiplexing (OFDM) are necessary. These techniques produce signals with significant amplitude variations, characterized by peak-to-average power ratio (PAPR). As a result, power amplifiers (PAs), as the most

Received 27 August 2024; revised 21 October 2024; accepted 9 November 2024. This work was supported in part by the National Science Foundation under Award 1914875 and Award 2218808. (Corresponding author: Kenle Chen.)

The authors are with the Department of Electrical and Computer Engineering, University of Central Florida, Orlando, FL 32816 USA (e-mail: pingzhu.gong@ucf.edu; kenle.chen@ucf.edu).

Color versions of one or more figures in this article are available at https://doi.org/10.1109/TMTT.2024.3497894.

Digital Object Identifier 10.1109/TMTT.2024.3497894

power-consuming components in wireless communication systems, experience considerable efficiency degradation. This is because a standalone PA without efficiency-enhancing technologies can only achieve maximum efficiency at its peak power output. In addition, with the advent of 5G communication, there are many available frequency bands (e.g., over 50 bands in the sub-6G range). The increasing breadth of the wireless spectrum necessitates that PAs operate across a wide frequency range.

To mitigate inefficiency in transmitting signals with high PAPR, several techniques have emerged as viable solutions. These include, but not limited to, envelop tracking (ET) [1], [2] and load modulation architectures such as outphasing PAs [3], [4], [5], [6], Doherty PAs (DPAs) [7], [8], [9], [10], [11], [12], [13], [14], [15], [16], [17], [18], and load-modulated balanced amplifiers (LMBAs) [19], [20], [21], [22], [23], [24], [25], [26], [27], [28], [29], [30], [31], [32], [33], [34], [35], [36], [37], [38], [39], [40], [41]. These advanced PA architectures offer high efficiency across various power levels, enhancing average efficiency when transmitting signals with high PAPR. Notably, within load-modulated PA architectures, DPA and LMBA can be implemented with a single input, making them particularly appealing.

DPA, initially proposed in [7], has been extensively studied and widely adopted in base station applications. However, its bandwidth is limited by the inherent constraints of the impedance inverter. Achieving impedance inversion requires a 90° transmission line, but the electrical length of the impedance inverter inevitably varies with frequency, making it impossible to consistently maintain the impedance inverting function. On the other hand, LMBA, first introduced in [19], has demonstrated the capability to provide wide bandwidth. By injecting an additional signal into the isolation port of the output quadrature coupler of the balanced amplifier (BA) through another control amplifier (CA), the efficiency of the BA is enhanced by load modulation. In addition, LMBA inherits the wideband nature of BA, offering a significant advantage over DPA. Initially, LMBA relied on dual inputs to freely adjust the phase of the control PA, thereby achieving wide bandwidth [19], [20]. Later, single-input wideband LMBAs were introduced [22], [23], demonstrating that it is

0018-9480 © 2024 IEEE. Personal use is permitted, but republication/redistribution requires IEEE permission. See https://www.ieee.org/publications/rights/index.html for more information.

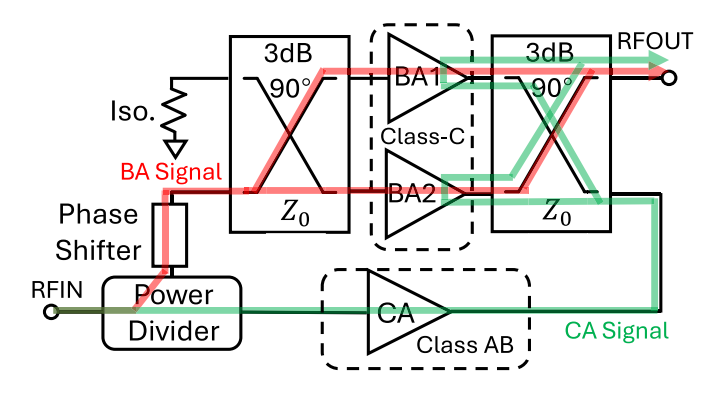


Fig. 1. General circuit schematic of PD-LMBA with signal paths.

possible to align the phase of LMBA without the need for an additional signal source. Furthermore, a re-engineered mode developed from the original LMBA has been proposed, named as the pseudo-Doherty LMBA (PD-LMBA) [24] or sequential LMBA (SLMBA) [25]. In PD-LMBA/SLMBA, the CA serves as the carrier PA and the BA as the peaking PA, as shown in Fig. 1, which provides an extended output power back-off (OBO) range. This LMBA mode has demonstrated an OBO range exceeding 10 dB and an ultrawide bandwidth of up to dual octaves (4:1) [26].

While LMBA has demonstrated broadband performance in extensive experiments, no existing theory rigorously explains its wideband nature. The current theory relies on the Zmatrix of the quadrature coupler derived at a single frequency, which does not apply across the entire band. Moreover, for a single-input LMBA, the primary factors limiting wideband operation—besides the bandwidth of the coupler and the transistor's cutoff frequency-include achieving proper phase alignment. The phase of the BA and CA signals is influenced by all LMBA building blocks and must satisfy certain conditions to enable the desired load modulation behavior. Currently, proper phase alignment of LMBA is achieved by sweeping the phase of the CA signal to obtain a set of phase values over frequency, followed by designing a phase shifter to realize the required phase profile [19], [24], [40]. Efforts have been made to consider the impact of the BA output matching network (OMN) on the broadband load modulation behavior [29], [30]. However, the existing theory does not account for the effects of all building blocks. Consequently, the design methodology for the phase shifter remains unclear, as it lacks a solid theoretical foundation.

In the microwave domain, the signal-flow graph is a powerful tool for addressing *S*-matrix-related problems. Using a signal-flow graph, the behavior of signals can be precisely visualized and analyzed. This approach has been used in the analysis of BAs [42], [43], and a preliminary analysis of the signal flow in LMBA was covered in our previous work [27]. To establish a generalized theory for the wideband operation of LMBA and provide a systematic solution to the phase-alignment problem, we will explore the *S*-matrix-based signal-flow approach, as an extension of our previous work [44]. It is worth noting that the signal-flow approach used in this article was initially inspired by a diagram from

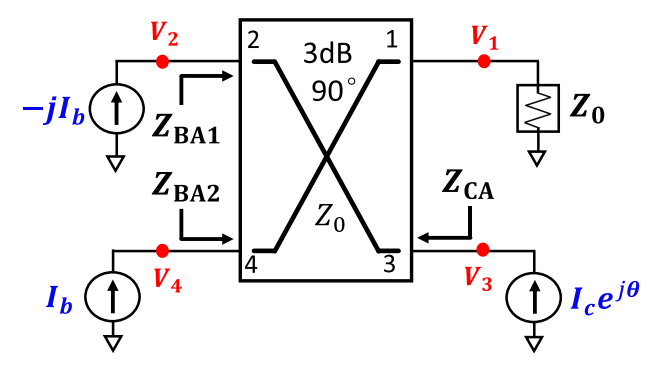


Fig. 2. Existing LMBA model with PAs represented as ideal current sources.

a lecture slide, which will be acknowledged accordingly in Acknowledgment. This approach allows us to account for the frequency-dependent characteristics of all LMBA building blocks using S-parameters, thereby enabling a systematic solution to the phase-alignment issue. In addition, the proposed theory demonstrates the consistent load modulation behavior of LMBA across the band and fundamentally explains its wideband nature. The theory and methodology are validated through the development of a PD-LMBA prototype. The bandwidth of the PD-LMBA prototype is expanded to an unprecedented decade, significantly outperforming the current state-of-the-art.

II. SIGNAL-FLOW-BASED BROADBAND LMBA THEORY

The RF-input LMBA described in Fig. 1 consists of a BA and a CA. To further illustrate the limitations of the existing LMBA theory, we will review the derivation process of the impedance equations for LMBA [19], [24] using the model depicted in Fig. 2. In the existing model, each PA is represented as an ideal current source, and the coupler is mathematically represented by its Z-matrix

$$\begin{bmatrix} V_1 \\ V_2 \\ V_3 \\ V_4 \end{bmatrix} = Z_0 \begin{bmatrix} 0 & 0 & -j & -j\sqrt{2} \\ 0 & 0 & -j\sqrt{2} & -j \\ -j & -j\sqrt{2} & 0 & 0 \\ -j\sqrt{2} & -j & 0 & 0 \end{bmatrix} \begin{bmatrix} I_1 \\ I_2 \\ I_3 \\ I_4 \end{bmatrix}$$
(1)

where $V_1 = -I_1/Z_0$, $I_2 = -jI_b$, and $I_4 = I_b$, representing the input RF currents from BA1 and BA2, while $I_3 = I_c e^{j\theta}$ denotes the CA current. In addition, the coupler is assumed to be realized by coupled lines. With these boundary conditions established, the impedance equations for the BA and the CA can be solved and expressed as follows:

$$Z_{\text{BA1}} = Z_{\text{BA2}}$$

$$= Z_0 \left(1 + \frac{\sqrt{2} I_c e^{j\theta}}{I_b} \right)$$
(2)

$$Z_{\text{CA}} = Z_0. \tag{3}$$

By biasing the CA and the BA in different PA modes (e.g., Class B for CA and Class C for BA in PD-LMBA), the currents of the CA and BA increase at different rates as the input power rises. This difference results in a changing ratio between the BA and CA currents across different power

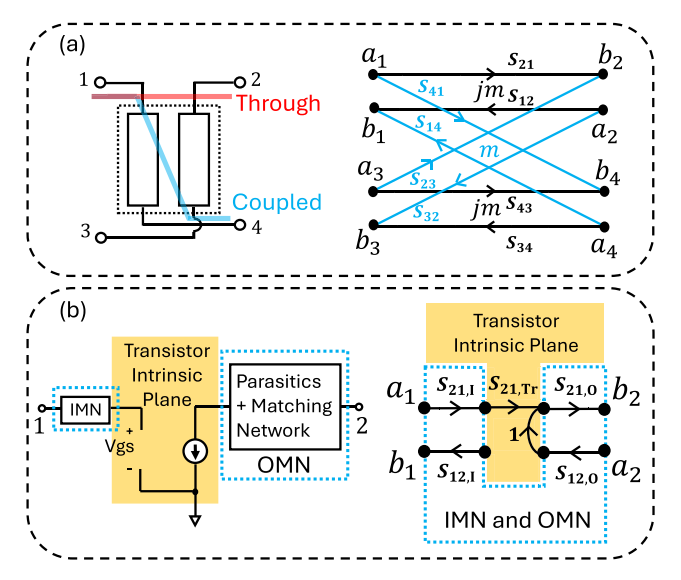


Fig. 3. Circuit schematics and signal-flow graphs of (a) wideband quadrature coupler and (b) standalone PA.

levels, eventually leading to impedance variations in (2) (i.e., $Z_{\rm BA}$ decreases as the input power increases). This is the load modulation mechanism of LMBA. Note that the quadrature coupler can also be realized by branch-line topology, and its Z-matrix [24] is slightly different from (1), where the elements "-j" are replaced by "+j." Nevertheless, the same impedance (2), (3) for LMBA can be derived for both the cases.

Despite providing a concise and accurate description of the load modulation behavior of LMBA, the existing theory has several significant drawbacks. First, the Z-matrix of the quadrature coupler, expressed by (1), is derived at a single frequency. As a result, it cannot rigorously explain the wideband nature of LMBA. Second, in the existing theory, each PA is represented as a current source. In practice, however, each PA requires an input matching network (IMN) and an OMN to function properly. These matching networks are frequency-dependent components, and their effects can significantly impact the load modulation behavior of LMBA, especially concerning the phase-alignment problem, a common challenge in LMBA design.

For example, in PD-LMBA as shown in Fig. 2, it is necessary to align the phase of the entire circuitry properly. This ensures that the relative phase of the CA current in (2) is zero across the entire band. Achieving zero phase offset results in a real BA impedance, which is essential for the proper operation of a PA according to loadline theory, minimizing voltage swing and preventing early saturation [45]. This, in turn, maintains the load modulation behavior of LMBA across the band. To achieve proper phase alignment, a phase shifter is required at the BA input to compensate for the phase delay introduced by each building block of the LMBA circuitry. However, the existing theory does not consider the effects of matching networks, making it unable to systematically address the phase-alignment problem, which is critical for ensuring the wideband operation of LMBA. We will address these challenges using the S-matrix-based signal-flow approach in this section.

A. Circuit Modeling With S-Matrix-Based Signal-Flow Graph

In a quadrature coupler, the signal is split equally between the through port and the coupled port with a phase offset of 90°. For a broadband quadrature coupler, although the phase offset between the two signal paths should remain a constant 90° across frequencies, the phase delay of each individual path is actually a frequency-dependent parameter, which may vary significantly across the band. To properly characterize these properties, the *S*-matrix of a lossless broadband quadrature coupler is given by

$$\begin{bmatrix} b_1 \\ b_2 \\ b_3 \\ b_4 \end{bmatrix} = \begin{bmatrix} 0 & jm & 0 & m \\ jm & 0 & m & 0 \\ 0 & m & 0 & jm \\ m & 0 & jm & 0 \end{bmatrix} \begin{bmatrix} a_1 \\ a_2 \\ a_3 \\ a_4 \end{bmatrix}$$
(4)

where $m = (1/\sqrt{2})e^{j\theta_{\text{Coupler}}(\omega)}$. The magnitude of m is $(1/\sqrt{2})$, denoting an equal power split between the through port and the coupled port. While the phase of m is denoted by $\theta_{\text{Coupler}}(\omega)$, representing its frequency dependence, the relationship S_{21} = jS_{41} consistently holds true. This implies that a 90° phase shift between the through and coupled ports can be maintained across the entire frequency range of the coupler [i.e., the amplitude and phase imbalance are neglected in (4)]. The previously derived S-matrix for the quadrature coupler in [46], where frequency variation is not considered, can be viewed as a special case of the S-matrix denoted by (4). On the other hand, the frequency-dependent S-matrix denoted by (4) corresponds to a frequency-dependent Z-matrix, which implies that the Z-matrix denoted by (1) is no longer valid for a broadband coupler. Note that (4) applies for both branch-line and coupled-line quadrature couplers. Specifically, $m = (-1/\sqrt{2})$ corresponds to a branch-line quadrature coupler, while m = $(-i/\sqrt{2})$ corresponds to a coupled-line quadrature coupler (single-section center frequency).

The S-matrix of the transistor in a PA is expressed as

$$[S_{\text{Tr}}] = \begin{bmatrix} 0 & 0 \\ S_{21,\text{Tr}} & 1 \end{bmatrix}. \tag{5}$$

The transistor is modeled as an ideal voltage-controlled current source with infinite reverse isolation, and it is assumed to be matched at the input. $S_{21,Tr}$ indicates the gain of the transistor. Furthermore, the *S*-matrix of input/output (I/O) matching network of a PA is represented as

$$[S_{I/O}] = \begin{bmatrix} 0 & S_{12,I/O} \\ S_{21,I/O} & 0 \end{bmatrix}.$$
 (6)

Both the IMN and OMN are assumed to be matched and reciprocal.

Based on the S-matrix of (4)–(6), the signal-flow graphs for the coupler and the PA are depicted in Fig. 3(a) and (b), respectively. Note that the device parasitics is considered as part of the OMN in (5) and (6).

B. LMBA Revisited Using Signal-Flow Graph

The full signal-flow graph for LMBA can be constructed by combining the signal-flow graphs of each individual block,

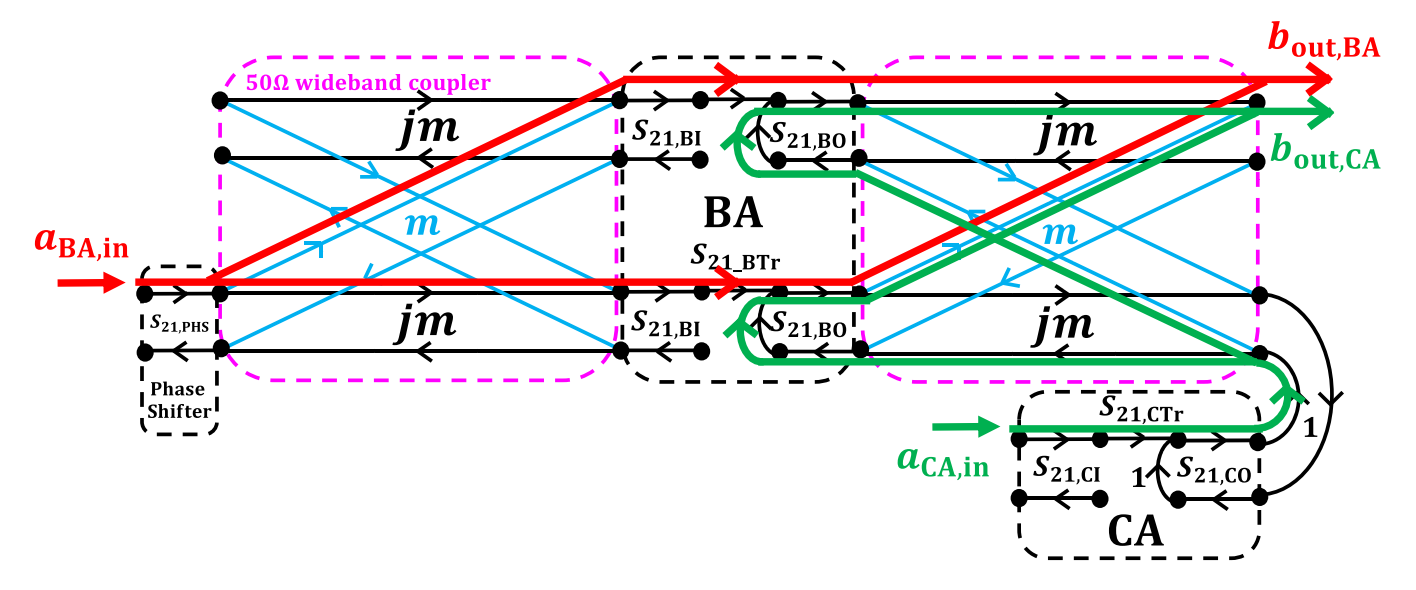


Fig. 4. Full signal-flow graph of LMBA showing BA (in red) and CA (in green) signal paths.

as indicated by Fig. 4. This graph can be viewed as the combination of one phase shifter, two couplers, and three sub-PAs, with IMN and OMN included. The *S*-matrix of the phase shifter can also be modeled by (6).

By applying Mason's rules [46] to the signal-flow graph of LMBA in Fig. 4, the BA and CA signal paths can be identified and visualized, similar to [27]. Starting from the input port before the phase shifter, the BA signal is evenly split into two paths upon encountering the input coupler. Subsequently, as the BA signals traverse the input coupler and respective BAs, they are recombined at the output coupler. Simultaneously, the CA signal, starting from the input port of CA, undergoes equal splitting at the isolation port of the output coupler. Intriguingly, the CA signal not only traverses CA's OMN but also traverses BA's OMN. After experiencing complete reflection at the intrinsic drain of BA, the CA signal then traverses BA's OMN once more. Following this intricate path, CA signals are ultimately recombined at the output of the coupler.

While additional loops and paths exist within the circuit, their effects elegantly cancel each other out, effectively rendering them inconsequential. This cancellation occurs due to two well-known properties of the quadrature coupler: First, when two BA signals pass through the output coupler, half of each signal will propagate to the isolation port with equal signal strength but an exact phase offset of 180°, resulting in perfect cancellation. Second, after the CA signals, injected from the isolation port, are reflected back at the BA drain, although part of each signal will be reflected to the isolation port, they will again cancel each other perfectly because they have equal strength and a 180° phase offset. These properties are valid as long as the frequency is within the bandwidth of the coupler, where (4) is satisfied.

The gains of these signal paths are quantitatively calculated as follows. The output waves $(b_{\text{out,BA}}, b_{\text{out,CA}})$ induced by the BA and CA inputs $(a_{\text{BA}}, a_{\text{CA}})$ can be expressed

as

$$b_{\text{out,BA}} = a_{\text{BA,in}} \cdot 2jm^2 S_{21,\text{PHS}} S_{21,\text{BI}} S_{21,\text{BTr}} S_{21,\text{BO}}$$

$$b_{\text{out,CA}} = a_{\text{CA,in}} \cdot 2jm^2 S_{21,\text{CI}} S_{21,\text{CTr}} S_{21,\text{CO}} S_{21,\text{BO}}^2$$
(7)

where $S_{21,PHS}$ stands for S_{21} of the phase shifter, and subscripts B and C refer to BA and CA, respectively (e.g., $S_{21,BI}$ denotes S_{21} of the BA IMN, and $S_{21,CTr}$ denotes S_{21} of the CA transistor). The total output wave is a combination of BA and CA, i.e., $b_{out} = b_{out,BA} + b_{out,CA}$. The common factor jm^2 implies that both the BA signal and CA signal pass through the coupler twice, resulting in the same phase delay. The shared factor $S_{21,BO}$ indicates that the BA signal passes through the BA OMN once, while the CA signal traverses the BA OMN twice.

To understand the load modulation mechanism of LMBA, we need to analyze the impedance seen by the BA drain. From an S-parameter perspective, the BA impedance can be characterized by the active reflection coefficient at the drain, $\Gamma_{\rm BA}$. $\Gamma_{\rm BA}$ is a function of the incident wave, $a_{1,{\rm Drain}}$, and the outgoing wave, $b_{1,{\rm Drain}}$. The term "active" indicates that $\Gamma_{\rm BA}$ varies with the power level of LMBA, which will be discussed next. From the previous analysis about the signal-flow graph of LMBA, BA signal and CA signal meet up with each other at the BA drain. This behavior is shown in Fig. 5, where the remaining portion of each path is hidden. It is interesting to note that the outgoing wave, $b_{1,{\rm Drain}}$, equals to the CA signal propagating to the BA drain, $b_{\rm CA}$

$$b_{1,\text{Drain}} = b_{\text{CA}}.$$
 (8)

Meanwhile, the incident wave $a_{1,Drain}$ is the combination of a_{BA} , the BA signal propagating to the BA drain, and b_{CA}

$$a_{1,\text{Drain}} = a_{\text{BA}} + b_{\text{CA}}.\tag{9}$$

When the CA signal passes through the intrinsic drain of the BA transistor, it can be considered as a "reflected" wave observed by the intrinsic drain, leading to a "mismatched" impedance characterized by Γ_{BA} , different from Z_0 . Γ_{BA} is expressed as

$$\Gamma_{\text{BA}} = \frac{b_{1,\text{Drain}}}{a_{1,\text{Drain}}}$$

$$= \frac{b_{\text{CA}}}{a_{\text{BA}} + b_{\text{CA}}}.$$
(10)

By varying the amplitude and the phase of the "reflected" wave (i.e., b_{CA}), Γ_{BA} takes different values, resulting in a changing BA impedance. This phenomenon is commonly known as load modulation.

Based on (10), the BA impedance can be written as

$$Z_{\rm BA} = \gamma_{\rm BA} Z_0 \left(1 + 2 \frac{b_{\rm CA}}{a_{\rm BA}} \right)$$
 (11)

where $\gamma_{\rm BA} Z_0$ represents the overall reference impedance at the BA drain, and $\gamma_{\rm BA}$ refers to the impedance transformation ratio of the BA OMN, which is connected to the output coupler with an impedance of Z_0 . Similar to (7), $b_{\rm CA}$ and $a_{\rm BA}$ can be expressed as

$$b_{\text{CA}} = a_{\text{CA.in}} \cdot S_{21.\text{CI}} S_{21.\text{CTr}} S_{21.\text{CO}} jm S_{21.\text{BO}}$$
 (12)

$$a_{\text{BA}} = a_{\text{BA,in}} \cdot S_{21,\text{PHS}} jm S_{21,\text{BI}} S_{21,\text{BTr}}$$
 (13)

where $\angle b_{\text{CA}} = \theta_{\text{CA}}(\omega)$ and $\angle a_{\text{BA}} = \theta_{\text{BA}}(\omega)$, denoting the frequency-dependent phase of each wave. To be consistent with the original LMBA theory, we will then replace b_{CA} and a_{BA} with the current at the BA intrinsic drain, I_{BA} , and the current at the CA intrinsic drain, I_{CA} , in (11). Converting arbitrary power waves into a current requires the following equation:

$$I = \frac{1}{\sqrt{Z_0}}(a-b) \tag{14}$$

where a and b stand for the incident wave and outgoing wave at one specific port, respectively. By plugging in (8) and (9) into (14), the amplitude relationship between I_{BA} and a_{BA} is given by

$$|I_{\rm BA}| = \frac{1}{\sqrt{\gamma_{\rm BA} Z_0}} |a_{\rm BA}|. \tag{15}$$

 $I_{\rm CA}$ can also be calculated using (14) based on the incident wave and the outgoing wave at the CA drain. Notably, in Fig. 4 there is no outgoing wave at the CA drain (i.e., b=0), and therefore, $I_{\rm CA}$ is only related to the incident wave. According to the signal-flow graph of LMBA in Fig. 4, the amplitude of $I_{\rm CA}$ can be expressed as

$$|I_{\text{CA}}| = \frac{1}{\sqrt{\gamma_{\text{CA}} Z_0}} |a_{\text{CA,in}} S_{21,\text{CI}} S_{21,\text{CTr}}|$$
 (16)

where $\gamma_{\rm CA} Z_0$ stands for the reference impedance at the CA drain, and $\gamma_{\rm CA}$ refers to the impedance transformation ratio of the CA OMN. While to derive the relationship between $I_{\rm CA}$ and $b_{\rm CA}$, some assumptions need to be made. For matched and lossless matching networks and couplers, we have $|S_{21,{\rm CO}}| = |S_{21,{\rm BO}}| = 1$ and $|jm| = (1/\sqrt{2})$. With these assumptions, by comparing (16) with (12) we have the following relationship:

$$|I_{\text{CA}}| = \frac{1}{\sqrt{\gamma_{\text{CA}} Z_0}} \sqrt{2} |b_{\text{CA}}|.$$
 (17)

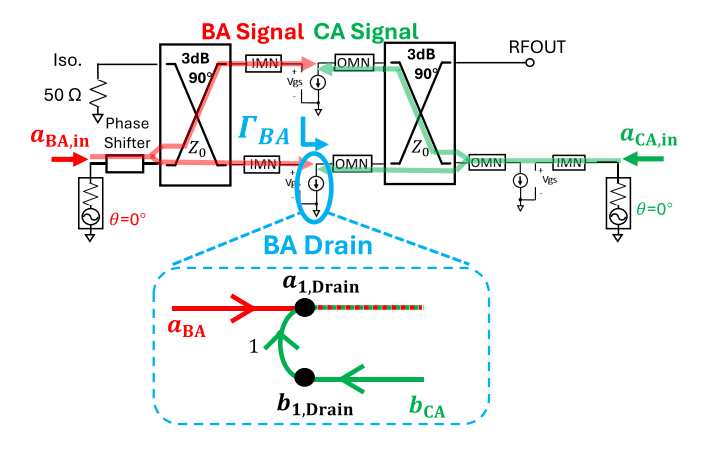


Fig. 5. Active reflection coefficient Γ_{BA} as a function of the BA signal and the CA signal.

Based on (15) and (17) while considering the phase of b_{CA} and a_{BA} , Z_{BA} in (11) can be rewritten as

$$Z_{\rm BA} = \gamma_{\rm BA} Z_0 \left[1 + \sqrt{2} \frac{|I_{\rm CA}|}{|I_{\rm BA}|} \sqrt{\frac{\gamma_{\rm CA}}{\gamma_{\rm BA}}} e^{j(\theta_{\rm CA}(\omega) - \theta_{\rm BA}(\omega))} \right]. \tag{18}$$

For the CA transistor, as there is no signal passing through its drain other than itself, the impedance observed by the CA drain is constantly matched (i.e., $\Gamma_{CA} = 0$). Z_{CA} is given by

$$Z_{\rm CA} = \gamma_{\rm CA} Z_0. \tag{19}$$

Equations (18) and (19) stand for the rederived impedance equations for LMBA. Note that (18) applies to both the BAs. Unlike the conventional LMBA theory, (18) and (19) involve the effect of all the building blocks of LMBA and is valid for all the in-band frequencies. Furthermore, in (18), the phase term, $[\theta_{CA}(\omega) - \theta_{BA}(\omega)]$, no longer refers to the relative phase of I_{CA} , but instead it represents the frequency-dependent phase offset between the BA signal path and the CA signal path at the BA intrinsic drain, where the CA signal actually passes through the BA OMN before. It is also important to emphasize that the impedance equations now apply directly to the BA and CA intrinsic drain instead of the coupler plane, and the reference impedances refer to the impedances provided by the OMNs at the drain, which means Z_{BA} and Z_{CA} can scale up and down according to the impedance transformation ratio, γ_{BA} and γ_{CA} [25].

To clarify a common misunderstanding about LMBA, the reason why the consistency of the load modulation behavior of $Z_{\rm BA}$, ideally, is not interrupted by BA OMN that has a fixed impedance transformation behavior, is as follows. Typically, OMN acts as an impedance transformer that operates effectively only when a constant load is present. Any deviation from this desired load (i.e., $\Gamma_L \neq 0$) causes part of the incident wave to reflect back at the load, pass through the OMN once again, and eventually appear as an outgoing wave at the input port, as indicated by Fig. 6(a). Subsequently, this nonzero outgoing wave leads to impedance mismatch. Especially for broadband operation, OMN highly depends on frequency, which leads to the phase difference between the outgoing wave and incident wave (i.e., the phase of Γ_{in}) being highly frequency-dependent. As a result, the original impedance transformation ratio of OMN is no longer valid for broadband operation when the load varies. However, this conventional analysis does not apply to LMBA. In LMBA, BA OMN is connected to the coupler followed by the CA, and any outgoing wave originates from the CA signal rather than a portion of the BA signal, as indicated by Fig. 6(b). This unique mechanism allows LMBA to independently control the amplitude and phase of the incident and outgoing waves. Consequently, $Z_{\rm BA}$ can exhibit the desired load modulation behavior as long as BA OMN is matched to the reference impedance of the coupler (e.g., 50 Ω) without the need to consider match the OMN to multiple values at different power levels, and provided that the phase difference between the BA and CA signals is properly selected.

C. Frequency-Agnostic Phase Alignment for PD-LMBA

Given the ideal load modulation behavior of PD-LMBA, (18) should provide a real value. This requires the following phase-alignment condition to be satisfied:

$$\theta_{\rm CA}(\omega) = \theta_{\rm BA}(\omega).$$
 (20)

With this condiction, Z_{BA} is expressed as

$$Z_{\rm BA} = \gamma_{\rm BA} Z_0 \left(1 + \sqrt{2} \frac{|I_{\rm CA}|}{|I_{\rm BA}|} \sqrt{\frac{\gamma_{\rm CA}}{\gamma_{\rm BA}}} \right). \tag{21}$$

This means PD-LMBA can exhibit desired load modulation behavior over different frequencies as long as the phase-alignment condition denoted by (20) is satisfied. To further clarify this condition, (20) can be rewritten as

$$\theta_{\text{Shifter}}(\omega) + \theta_{\text{IMN,BA}}(\omega) + \theta_{\text{Device}}(\omega)$$

$$= \theta_{\text{OMN,BA}}(\omega) + \theta_{\text{OMN,CA}}(\omega) + \theta_{\text{Device}}(\omega) + \theta_{\text{IMN,CA}}(\omega)$$
(22)

where the frequency-dependent phase delay of each building block is included (e.g., $\theta_{\text{Shifter}}(\omega) = \angle S_{21,\text{PHS}}$). Equation (22) implies the BA signal and CA signal should be in-phase combined at the BA drain, as shown in Fig. 7, to provide a real Γ_{BA} and consequently a real Z_{BA} . Remarkably, both the BA signal and the CA signal, before being combined at the BA drain, pass through the same quadrature coupler once. Therefore, the phase delay induced by $\theta_{\text{Coupler}}(\omega)$ is canceled out within the band, even though $\theta_{\text{Coupler}}(\omega)$ is a function of frequency. This unique mechanism implies that LMBA, much like a BA, uses the coupler in a somewhat balanced way, which is a key feature for ensuring the broadband operation. This also indicates that the input coupler should ideally be identical to the output coupler to provide the same $\theta_{\text{Coupler}}(\omega)$ for the BA and CA signal paths over the entire band to ensure the phase cancellation. Due to the consistent in-phase combination of BA and CA signals at the intrinsic drain across all the frequencies, the impedance seen by the BA transistor will consistently be "mismatched" by the same amount, ensuring broadband load modulation behavior. Especially, the CA signal path contains more building blocks. This is why we always need to add a phase shifter at the BA input to compensate for the delay and enforce phase equalization.

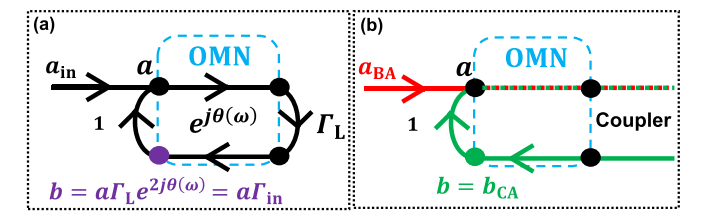


Fig. 6. Signal-flow graphs of (a) OMN terminated with a load Γ_L and (b) BA OMN in LMBA.

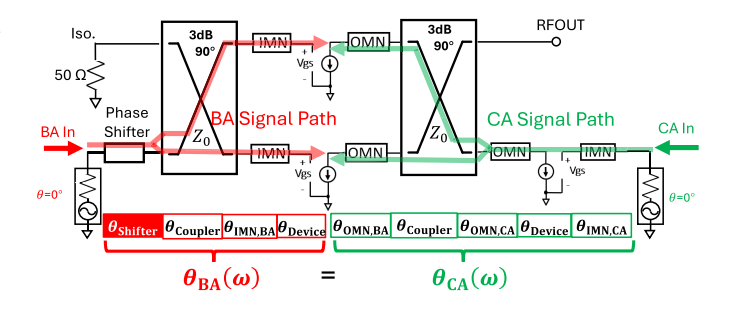


Fig. 7. Phase-alignment condition for PD-LMBA.

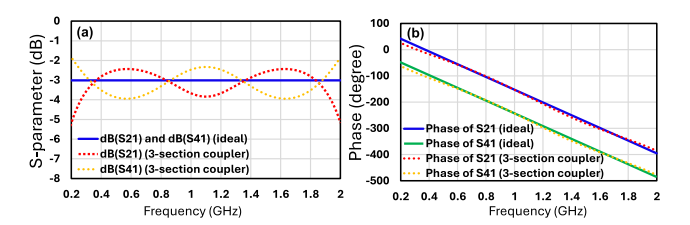


Fig. 8. Comparison between an ideal coupler indicated by (4) and a coupler realized by a three-section coupled line showing (a) amplitude and (b) phase of S-parameters from 0.2 to 2 GHz.

III. VERIFICATION USING IDEAL PD-LMBA MODEL

As discussed in Section II, the condition described by (22) leads to optimal load modulation behavior of PD-LMBA across the band. To verify this broadband phase-alignment condition, an ideal PD-LMBA circuit is simulated using Advanced Design System (ADS). The verification is conducted for two cases. In the first case, the matching networks are realized by transmission lines, which have a linear phase delay response over frequency. In the second case, the matching networks are realized by multisection low-pass topologies, which have a nonlinear phase delay response over frequency. In both the cases, the transistors are represented by ideal voltage-controlled current sources, and ideal broadband couplers indicated by (4) are used. The entire circuit is simulated in an optimal scenario to eliminate the impact of nonideal transistors, matching networks, and couplers.

The ideal broadband coupler described by (4) is verified by comparing its S-parameters with those of a three-section coupled-line coupler, as depicted in Fig. 8. The amplitude of S_{21} (i.e., jm) and S_{41} (i.e., m) for the ideal case is constantly equal to -3 dB, as depicted in Fig. 8(a). The phase of m is defined as a linear function of frequency, which closely mirrors the phase delay response of an actual three-section coupler that varies vastly over frequency, as shown in Fig. 8(b). Nevertheless, as discussed in Section II, $\theta_{\text{Coupler}}(\omega)$, whether

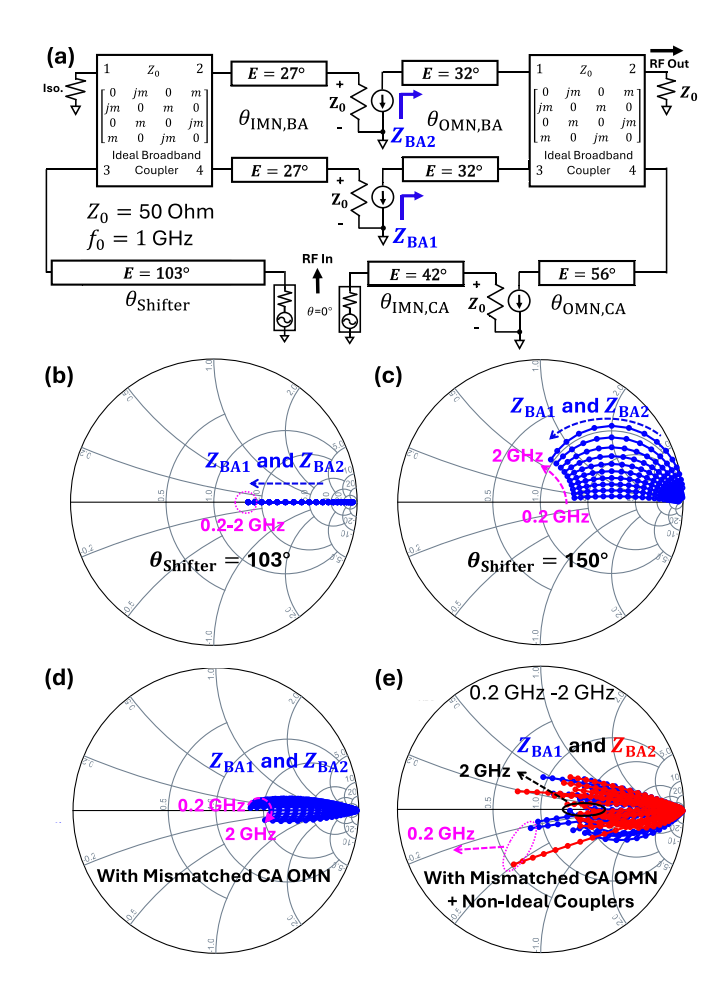


Fig. 9. (a) Circuit schematic of an ideal PD-LMBA with transmission—line-based matching networks and phase shifter. Load trajectories of BA when (b) phase-alignment condition is satisfied, (c) phase-alignment condition is violated, (d) mismatched CA OMN is used, and (e) mismatched CA OMN and nonideal couplers are used.

linear or nonlinear, is canceled out for the BA and CA signal paths, and hence has no impact on the load modulation behavior.

A. Verification of the Phase-Alignment Condition With Transmission-Line-Based Matching Networks and Phase Shifter

The circuit schematic of an ideal PD-LMBA is shown in Fig. 9(a), where the matching networks are realized by ideal transmission lines. The characteristic impedance of the transmission lines, couplers, and the input impedance of the transistor is chosen to be 50 Ω to enforce the broadband matching condition. The electrical length of each transmission line at 1 GHz is also indicated in Fig. 9(a). These electrical lengths are properly selected to satisfy the phase-alignment condition described by (22) (i.e., $103^{\circ} + 27^{\circ} = 42^{\circ} + 56^{\circ} + 32^{\circ}$). The entire circuit is simulated from 0.2 to 2 GHz at various power levels, and the trajectories of Z_{BA} are plotted, as depicted in Fig. 9(b). Z_{BA} decreases from infinity to a finite number along the real axis as the power increases, and identical load modulation behavior can be observed over the entire band, as expected from (21). The θ_{Shifter} is then

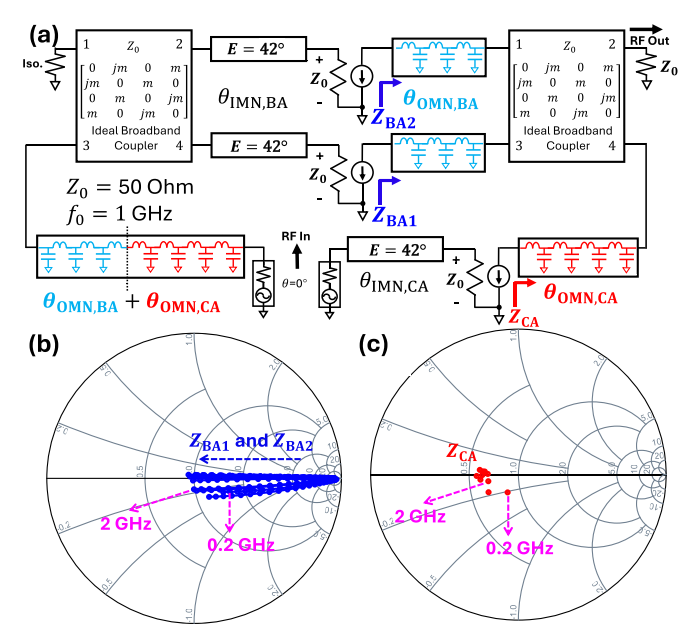


Fig. 10. (a) Circuit schematic of an ideal PD-LMBA with low-pass matching networks and phase shifter. (b) Load trajectories of BA when the phase-alignment condition is satisfied. (c) Load impedance of CA when the phase-alignment condition is satisfied.

set to 150° to violate the phase-alignment condition, and the simulated Z_{BA} is shown in Fig. 9(c). Obviously, Z_{BA} is no longer real and varies across the band, because the BA signal and the CA signal are not in-phase combined at the BA intrinsic drain. There are other factors that could cause the nonideal load trajectories. One factor is the mismatch of OMN. Another factor is the nonideal coupler. For example, if the CA OMN is replaced with a 100- Ω transmission line, the variation in Z_{BA} can be observed from Fig. 9(d). If we further replace the ideal broadband couplers with practical threesection couplers, which have a 2-dB amplitude imbalance as shown in Fig. 8, more variation in Z_{BA} can be observed from Fig. 9(e). The reason is that both nonideal couplers and mismatched networks can create additional loops and paths in the LMBA signal-flow graph, resulting in the variation in the amplitude and phase correlation between BA and CA signals, which eventually leads to the variation in Z_{BA} .

B. Verification of the Phase-Alignment Condition With Low-Pass Matching Networks and Phase Shifter

The matching circuit and phase shifter are then replaced by low-pass networks realized by capacitors and inductors, as shown in Fig. 10(a). To simplify the phase-alignment condition, the IMN of BA and CA is assumed to be identical (i.e., $\theta_{\text{IMB,BA}} = \theta_{\text{IMN,CA}}$). With this assumption, the phase-alignment condition described by (22) can be simplified as

$$\theta_{\text{Shifter}}(\omega) = \theta_{\text{OMN,BA}}(\omega) + \theta_{\text{OMN,CA}}(\omega).$$
 (23)

The OMN of BA is realized by a three-section low-pass circuit with an impedance transformation ratio of 30:50 Ω , while the CA OMN is realized by a four-section low-pass circuit with the same impedance transformation ratio. To satisfy the phase-alignment condition described by (23), the phase shifter

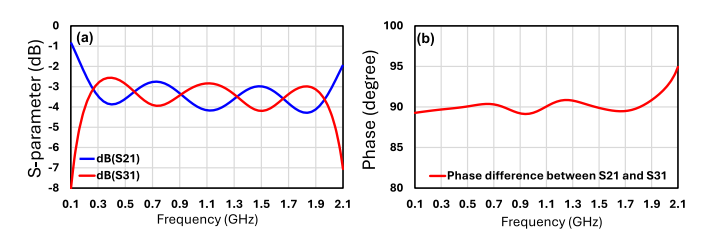


Fig. 11. (a) Amplitude and (b) phase of IPP-7116 from 0.2 to 2 GHz.

is constructed by directly combing the BA OMN and the CA OMN, as shown in Fig. 10(a). The entire circuit is simulated from 0.2 to 2 GHz at various power levels, and the trajectories of $Z_{\rm BA}$ are plotted, as depicted in Fig. 10(b). Similarly, almost identical load modulation behavior can be observed over the entire band, and $Z_{\rm BA}$ is scaled down to the lower values compared with Fig. 9(b) because of the lower impedance transformation ratio, as expected from (21). $Z_{\rm CA}$ is plotted in Fig. 10(c), which is around 30 Ω across the band. Note that the variation in $Z_{\rm BA}$ and $Z_{\rm CA}$ is purely caused by the mismatch of OMNs of the BA and CA.

IV. DESIGN OF DECADE-BANDWIDTH PD-LMBA

The target frequency range is from 0.2 to 2 GHz to showcase the ultrabroadband potential of PD-LMBA using the proposed theory, and the target OBO is set to 10 dB to accommodate high-PAPR signals. To construct the PD-LMBA circuit, a 10-W GaN transistor (MACOM CG2H40010F) is used for realizing the CA for its robust efficiency performance, especially in the low-power region. Two 15-W GaN transistors (MACOM CGHV27015S) are used for the BA to provide a high power back-off and a high gain, which will be discussed later. Two identical $50-\Omega$ wideband couplers (IPP-7116, Innovative Power Products) are used at the input and output of the BA to cover the frequency range from 0.2 to 2 GHz and provide the same phase delay for both BA and CA signal paths. Within the bandwidth of IPP-7116 from 0.2 to 2 GHz, the amplitude imbalance is around 1-dB, and the phase imbalance is less than 3°, as shown in Fig. 11. The circuit is electromagnetically (EM) simulated in ADS based on a 31-mil thick Rogers Duroid-5880 PCB board with a dielectric constant of 2.2.

A. Accurate Parasitic Network Estimation Using Comparative Method

In a realistic transistor, as depicted in Fig. 12(a), parasitic effects are unavoidable, which are caused by the drain–source p-n junction capacitance, $C_{\rm ds}$, and the package of the device. Device parasitics significantly affect the performance of a PA and should be characterized properly. Nowadays, many foundry models provide the access to the intrinsic node of a transistor, making it much easier to extract device parasitics. It is also possible to model a device without intrinsic nodes based on small-signal simulation, as demonstrated in [47]. Based on the intrinsic voltage and current at current source reference plane (CRP), $V_{\rm ds,int}$ and $I_{\rm ds,int}$, together with the voltage and current at the package reference plane (PRP), $V_{\rm ds,pkg}$ and $I_{\rm ds,pkg}$, the Z-matrix of parasitics can be calculated [48], where the embedding model [49] is used instead of the

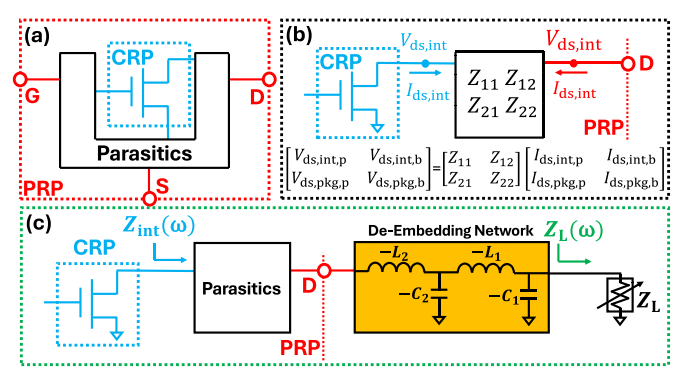


Fig. 12. (a) Realistic transistor with parasitics. (b) Parasitics extraction using Z-matrix [48]. (c) Proposed extraction method.

foundry model, as shown in Fig. 12(b). Note that this method requires two groups of voltage and current at different power levels since the Z-matrix has four unknown parameters. With the extracted Z-matrix at different frequencies, a simple LC network can be established to represent parasitics using curve fitting [48]. The drawbacks of this method are as follows. First, it requires the designer to export data to another software, MATLAB, for example, to perform the calculations. Second, if the parasitic network is complex, more effort is needed to set up the curve fitting.

Alternatively, device parasitics can be extracted directly in ADS simulation without the need to export data. The proposed method uses a well-known de-embedding network, an LC-based circuit [50] with negative capacitors and inductors, connected to a certain load $Z_L(\omega)$, as shown in Fig. 12(c). By tuning the values of L_1 , L_2 , C_1 , and C_2 of the deembedding network, device parasitics should be canceled out perfectly, which enforces the following equation:

$$Z_{\rm int}(\omega) = Z_L(\omega)$$
 (24)

where $Z_{\rm int}$ stands for the impedance observed by the intrinsic drain and can be calculated by taking the ratio between $V_{\rm ds,int}$ and $I_{\rm ds,int}$. Specifically, for a PA designer, (24) should be satisfied at fundamental, second-harmonic, and third-harmonic frequencies of the band to ensure the accuracy of the model. When (24) is observed from the simulation results, the parasitic model can be constructed by directly flipping the corresponding de-embedding network and the signs of inductors and capacitors. The parasitic model can also be extracted by comparing the waveform of voltage and current at CRP with the waveform at the load, and these waveforms should overlap with each other precisely.

Based on the proposed method, the parasitic models for CG2H40010F and CGHV27015S are extracted as shown in Fig. 13(a) and (b), respectively. The fundamental impedances are set to be 30 and 50 Ω . The impedances at harmonic frequencies are set to be short. The circuit is simulated using large-signal analysis from 0.2 to 2 GHz at various power levels, and (24) is enforced at fundamental, second, and third-harmonic frequencies, as depicted in Fig. 13. The de-embedding network is further verified by comparing the waveform of voltage and current at CRP with the load waveform at various power levels in Fig. 13(c).

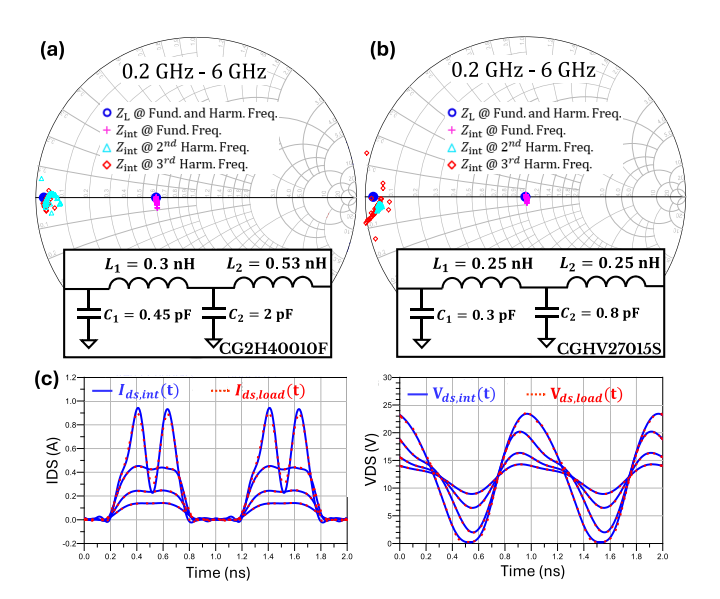


Fig. 13. (a) Extracted parasitic model for CG2H40010F. (b) Extracted parasitic model for CGHV27015S. (c) Comparison of the voltage and current waveforms at CRP and the load.

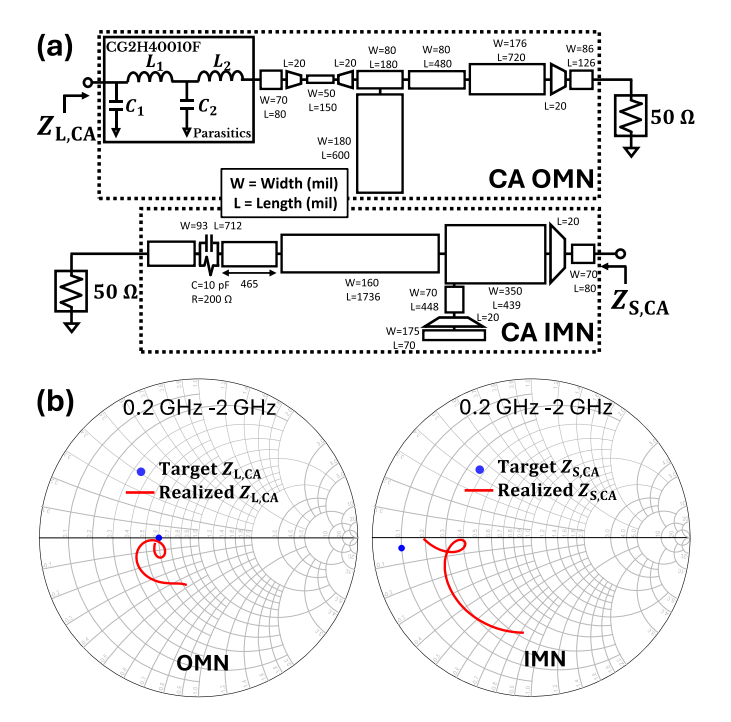


Fig. 14. (a) Circuit schematic of CA OMN and IMN. (b) Simulated matching results of CA.

B. Ultrabroadband CA Design

The schematics of the CA IMN and OMN, along with their dimensions, are depicted in Fig. 14(a). The target impedance for the OMN, $Z_{L,CA}$, is set to 30 Ω to achieve a good balance among power, efficiency, and bandwidth. To establish the broadband 30–50- Ω matching, a shunt open stub is placed immediately after the transistor drain, followed by two series transmission lines [10]. The extracted device parasitics are incorporated as part of the OMN, and the EM simulation result is shown in Fig. 14(b). For the IMN design, the optimum impedance is determined to be 5-2j based on source—

pull results. This impedance is chosen to provide high and consistent gain across the band. However, in the realistic design, achieving the target impedance across the entire band is challenging. Conversely, the IMN is not very sensitive to mismatch, especially at lower frequencies where the transistor intrinsically has a higher maximum available gain (MAG). A multisection-transformer-based matching network is used to realize the CA IMN, and the impedance at the CA gate, $Z_{S,CA}$, is designed to be close to the target impedance primarily in the upper portion of the band (1-2 GHz), as depicted in Fig. 14(b). An RC-based network (with $R = 200 \Omega$ and C = 10 pF) is integrated into the IMN to stabilize the CA. Importantly, based on the physical size of the transistors, RF-choke inductors, and couplers, their pads are included as part of the design as they may significantly impact the matching quality, especially for a broadband design.

C. Ultrabroadband BA Design

The schematics for the BA IMN and OMN and their dimensions are depicted in Fig. 15(a). After the back-off point, the majority of the power is generated by BA, and therefore, two 15-W GaN transistors (MACOM CGHV27015S) are chosen for the BA to provide high OBO. Other than power generation, the drain dc voltage required by these transistors is 50 V, and this leads to an optimum impedance around 60 Ω , after considering a knee voltage of 8 V. This optimum impedance fits well with 50- Ω couplers, especially it does not require a high-impedance transformation ratio for OMN design, which could limit the bandwidth. Furthermore, assuming a transformation ratio of 50:50 Ω from the BA OMN (i.e., $\gamma_{\rm BA}=1$), (21) indicates that $Z_{\rm BA}$ is naturally higher than the coupler impedance, Z_0 .

The target impedance for the BA, $Z_{L,BA}$, is set to 50 Ω to simplify the OMN design. Furthermore, CGHV27015S is packaged with surface-mount (SMT) and dual-flat-no-lead (DFN) technologies, and therefore, the impact of package parasitics is minimized. These factors enable us to realize the ultrawideband OMN with just a short transmission line, as depicted in Fig. 15(a). The EM simulation result is shown in Fig. 15(b). For the BA IMN design, the optimum impedance is set to 14 + 13j based on source—pull results. Ideally, this impedance can provide high and consistent gain across the band. However, it is hard to realized the target impedance across the entire band. Similar to CA, a multisection-transformer-based matching network is used to realize the BA IMN, and the impedance at the BA gate, $Z_{S,BA}$, is designed to be close to the target impedance primarily in the upper portion of the band (1–2 GHz), as depicted in Fig. 15(b). An RC-based network (with $R = 200 \Omega$ and C = 10 pF) is integrated into the IMN to stabilize the BA. The pads for the transistors, RF-choke inductors, and couplers are also included as part of the design.

D. Ultrabroadband Phase Alignment

As discussed in Section II, BA and CA signals should be in-phase combined at the BA drain to provide a real Γ_{BA} and subsequently a real Z_{BA} , which is essential for a PA to achieve

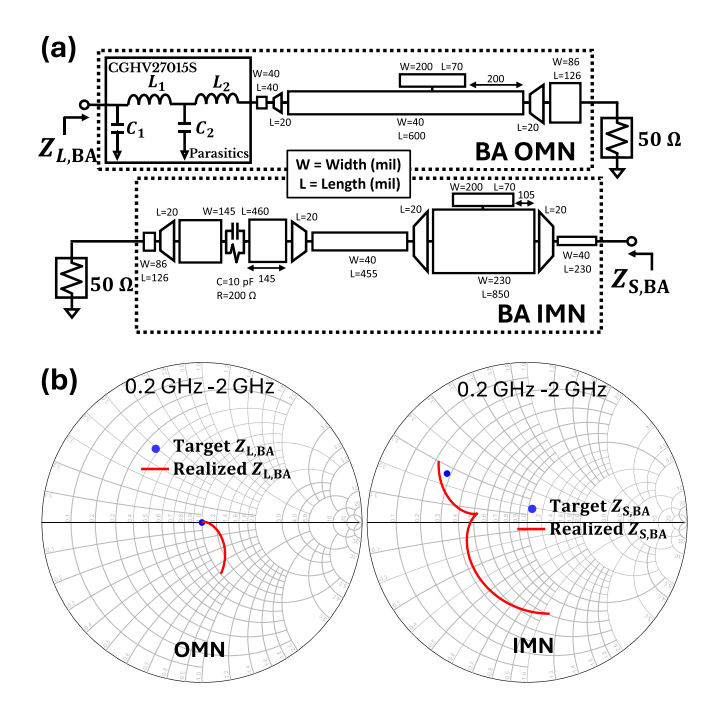


Fig. 15. (a) Circuit schematic of BA OMN and IMN. (b) Simulated matching results of BA.

maximized power and efficiency. To meet this phase-alignment condition, the IMNs and OMNs for both BA and CA are designed with the minimum number of shunt stubs to minimize phase dispersion, thereby simplifying the phase-alignment requirement. This results in the scenario shown in Fig. 9, where the phase delay response of all the matching networks is nearly linear over frequency. Consequently, a transmission-line-based phase shifter can be added at the BA input to properly align the phases of the BA and CA paths without needing a complex filter-based phase shifter.

To determine the length of the phase shifter, the phase delay response of the BA and CA signal paths is simulated using the circuit schematic shown in Fig. 16(a). The schematic is constructed based on (20)–(22) and Fig. 7. Both the input coupler and the output coupler are not included in the schematic, as the phase delay induced by the couplers cancels out for both the paths. Notably, device parasitics are considered as part of the BA OMN, and a de-embedding network is added after the BA transistor to access the intrinsic drain. The phase of the BA and CA signals at the BA drain is measured using $\angle S_{21}$. The length of the phase shifter is then determined to be 4600 mil to enforce the phase-alignment condition described by (20). The small-signal phase offset between the BA and CA signals is plotted in Fig. 16(b1), revealing that the phase difference in the proposed PD-LMBA is below 30° from 0.2 to 2 GHz. The large-signal phase difference is then plotted based on harmonic balance (HB) simulation, as shown in Fig. 16(b2). This phase difference increases in the high-power region due to the nonlinearity of the transistors. Fig. 16(b) displays the intrinsic load trajectories of BAs based on the intrinsic nodes provided by the foundry model, indicating a desired load modulation behavior across all in-band frequencies. The variation in load trajectories is primarily caused by the amplitude imbal-

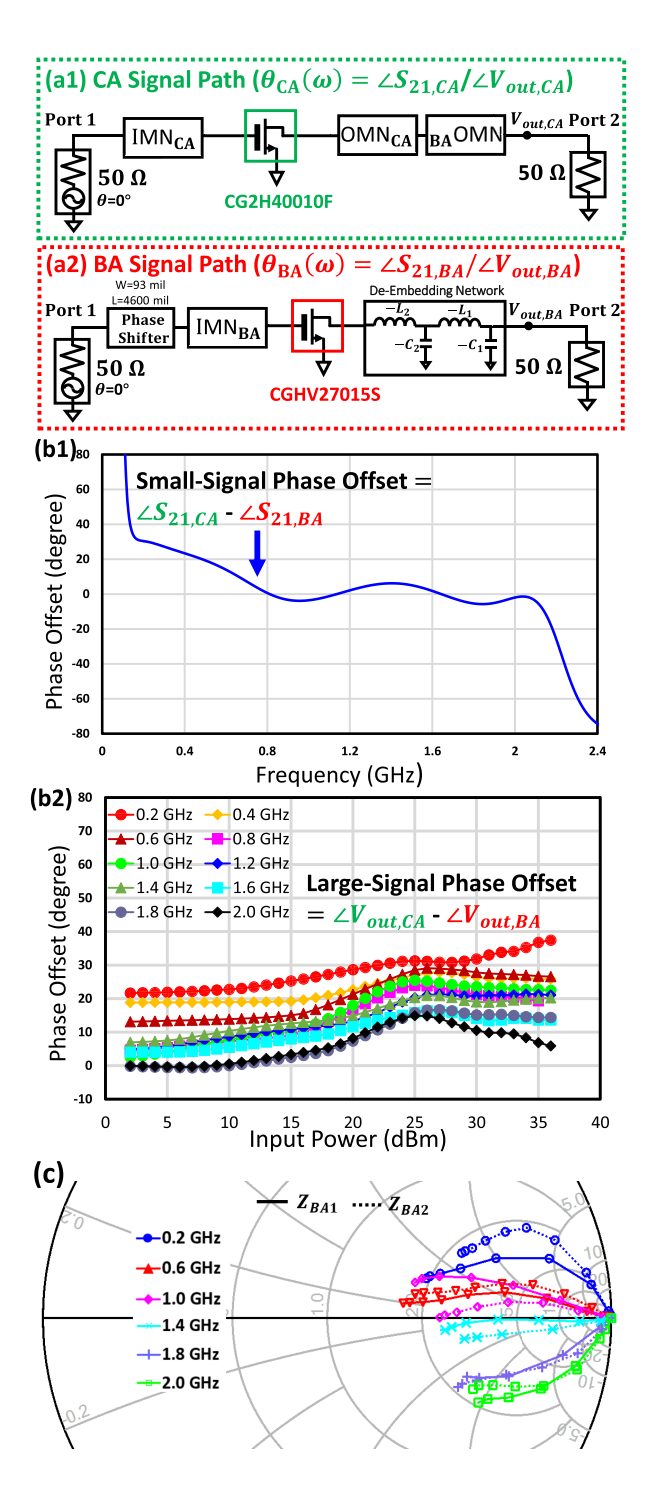


Fig. 16. (a) Simulation setup for measuring the phase delay response of the BA and CA signal paths. (b) BA and CA signal paths' phase offset at different frequencies across different power levels. (c) BA intrinsic load impedance trajectories.

ance of the coupler, nonideal matching networks, and transistor nonlinearities.

E. Overall Schematic and Simulation Results

The overall circuit schematic is shown in Fig. 17. A two-section Wilkinson power divider is designed to cover the target frequency range from 0.2 to 2 GHz. The physical sizes of the

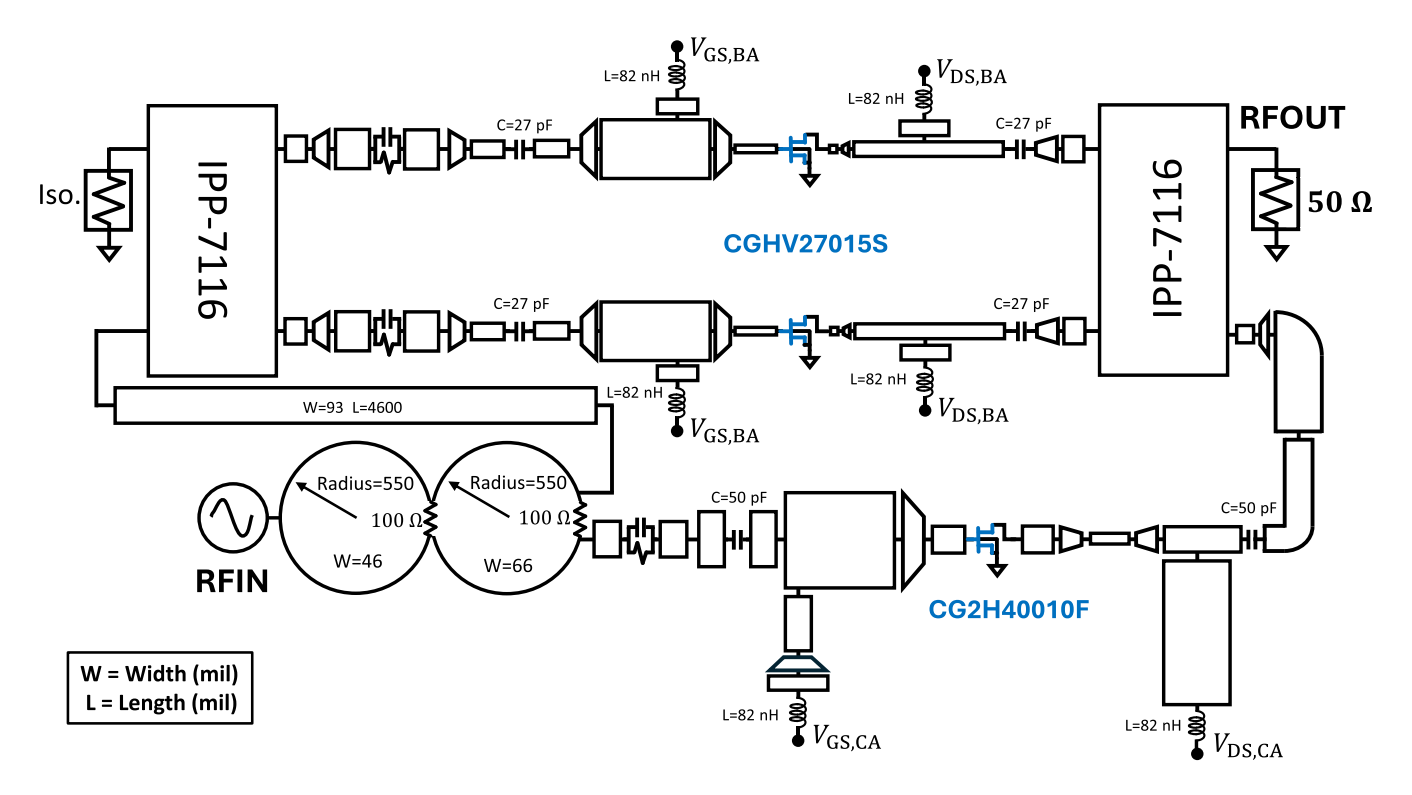


Fig. 17. Circuit schematic of decade-bandwidth PD-LMBA.

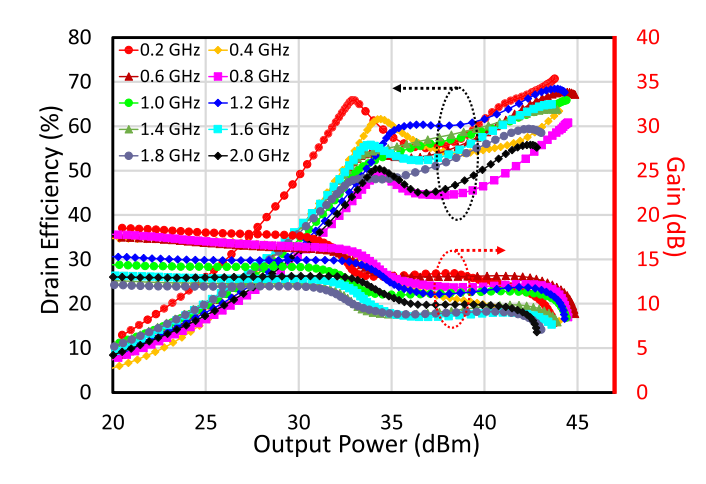


Fig. 18. Simulated efficiency and gain from 0.2 to 2 GHz.

matching networks are already included in Figs. 14 and 15. To bias the PA, high-Q inductors (Coilcraft 1515SQ-82N) are used in the circuit, with several dc-block capacitors added. Although the self-resonant frequency (SRF) of these inductors is within the band (1.79 GHz), they still effectively block the RF signals by providing high impedance, particularly since the impedance is near infinite at SRF. The CA is biased in Class-AB with $V_{\rm DD,CA}$ around 12 V. The BA is biased in Class-C with 50-V $V_{\rm DD,BA}$. High-power transistors are used for the BA, which allows the CA transistor to have a higher $V_{\rm DD,CA}$ for a given OBO, leading to improved gain. Furthermore, bias voltages ($V_{\rm GS}$) are adjusted to improve the PA performance at different frequencies. With the detailed design described in this section, the overall efficiency and

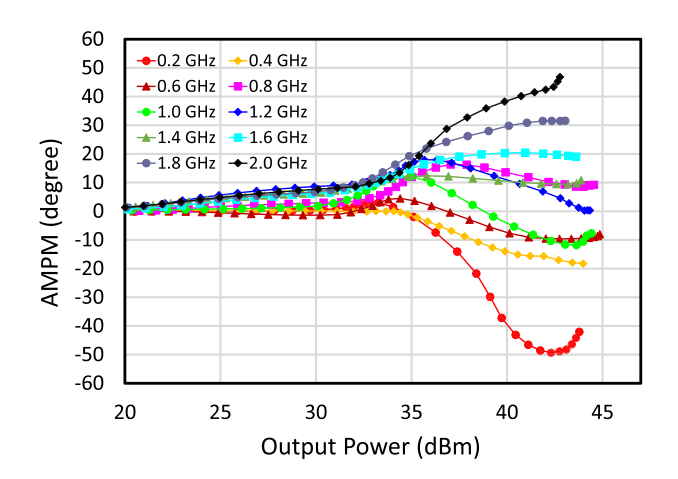


Fig. 19. Simulated AMPM from 0.2 to 2 GHz.

gain are swept with power based on EM simulation, as shown in Fig. 18. The results demonstrate strong load modulation behavior and efficiency enhancement over the entire band. The amplitude-to-phase distortion (AMPM) of the PD-LMBA is plotted in Fig. 19. The nonlinear behavior of the circuit is caused by the overdriving issue of the CA, which induces some nonlinear behavior of the carrier transistor.

V. IMPLEMENTATION AND EXPERIMENTAL RESULTS

The PA is implemented on a 31-mil-thick Rogers Duroid-5880 PCB board with a dielectric constant of 2.2, and the realized circuit is shown in Fig. 20. The prototype is tested using both continuous-wave (CW) and modulated signals.

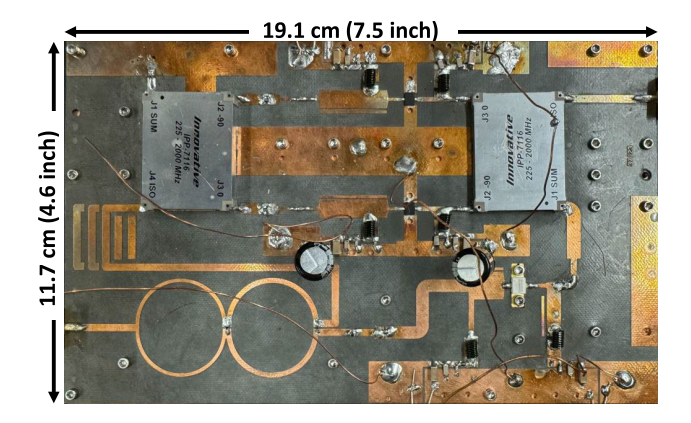


Fig. 20. Fabricated PD-LMBA prototype.

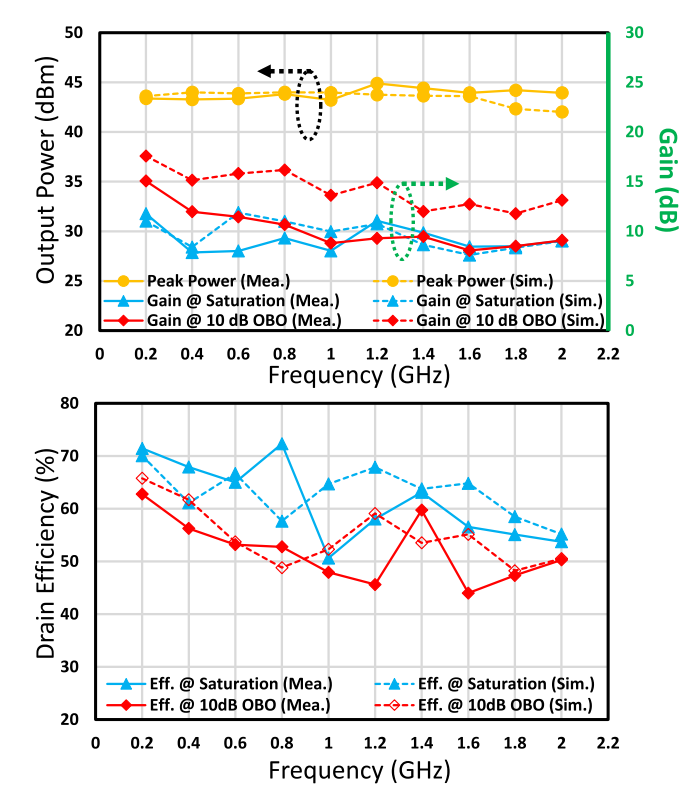


Fig. 21. Measured versus simulated output power, gain, and efficiency at various power levels from 0.2 to 2 GHz.

A. Continuous-Wave Measurement

The PD-LMBA prototype is evaluated using a single-tone signal across the frequency range of 0.2-2 GHz at various power levels. The frequency response is compared with the simulation results, as shown in Fig. 21. A peak output power ranging from 43 to 45 dBm is observed across the entire bandwidth, along with a gain of 9-15 dB at different OBO levels. The corresponding measured peak efficiency falls within the range of 51%-72%, and the efficiencies at 10-dB OBOs are in the range of 44%-62%. The power-dependent gain and efficiency profiles at various frequencies are shown in Fig. 22, which indicates a strong efficiency enhancement across different power levels. $V_{\rm GS,BA1}$ and $V_{\rm GS,BA2}$ are set unequal at some frequencies to further improve the back-off efficiency between the peak power and 10-OBO [51], e.g.,

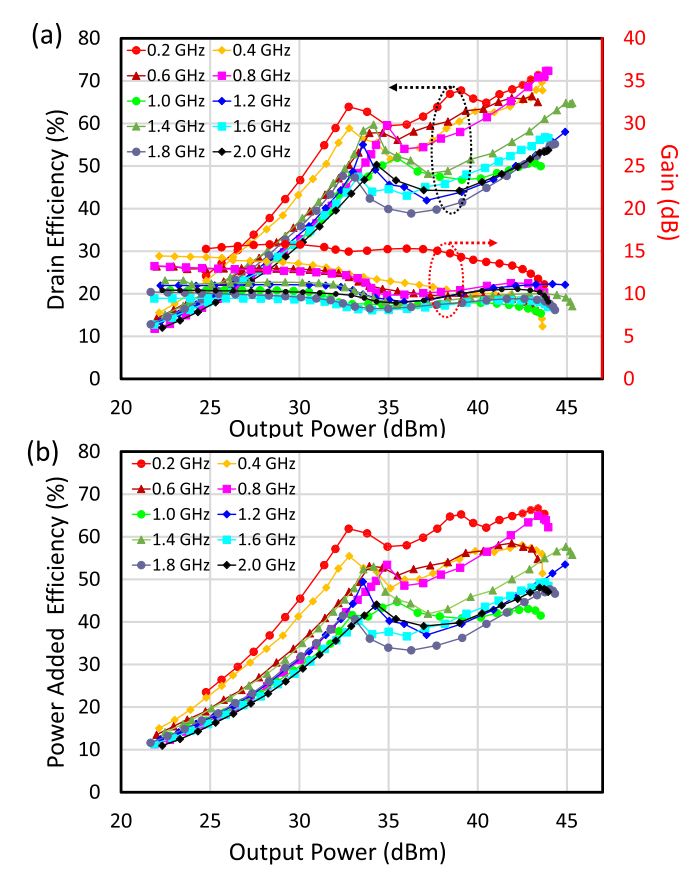


Fig. 22. (a) Power-swept measurement of drain efficiency and gain from 0.2 to 2 GHz. (b) Measured power-added efficiency.

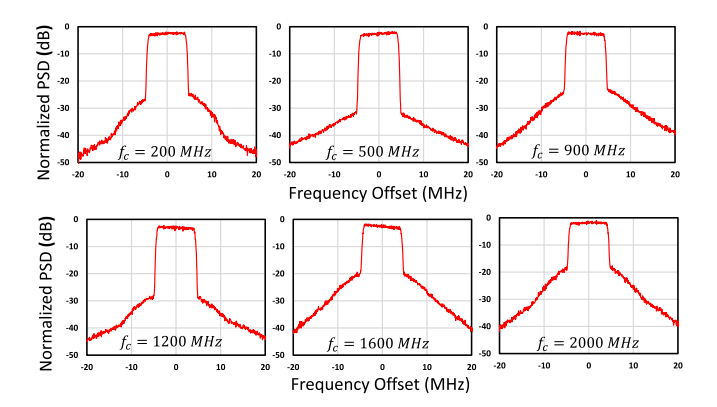


Fig. 23. Output spectrum from modulated measurements using a 10-MHz 10-dB-PAPR 5G NR signal centered at various frequencies across the band.

0.2 GHz in Fig. 22. Compared with the simulation results, the efficiency of the PD-LMBA prototype shows a slight degradation, while the gain drops by around 2–3 dB in the low-power region. This discrepancy is likely due to inaccuracy in the device model, particularly because the CA transistor is biased with $V_{\rm DD,CA}$ around 12 V, whereas the CG2H40010F model has its highest accuracy at 28 V. In addition, fabrication variations in the PCB board and couplers may also contribute to this discrepancy.

Table I presents a comparison between this design and other recently published DPAs and LMBAs. It is important

Ref. / Year	Architecture	Freq. (GHz)	f_{high}/f_{low}	Gain (dB)	P_{max} (dBm)	DE @ P_{max} (%)	DE @ 10-dB <i>OBO</i> (%)
[10] 2018	DPA	1.5-3.8	2.5	10-14	42-43	42-63	25-46*
[11] 2021	DPA	1.4-2.5	1.8	12-16	44-46	61-75.5	44.6-54.6
[18] 2019	DPA	1.6-2.6	1.6	8-10	45.5-46	53-66	50-53
[19] 2020	LMBA	1.5-2.7	1.8	8-12*	43	58-72	47-58
[26] 2021	LMBA	0.55-2.2	4	8-17*	41-43	49-82	39-64
[28] 2023	LMBA	2.05-3.65	1.8	8-11	45-47	61-80	51-66
[29] 2023	LMBA	1.3-2.1	1.6	-	50-53	28-62	42-53
[30] 2020	LMBA	1.45-2.45	1.7	11.2-13.4	45.6-46.7	67.1-77.9	40-47*
[39] 2024	LMBA	1.7-2.9	1.7	10-13*	40-42.9	56.8-72.9	47.1-64.8
[42] 2024	LMBA	1.9-3.2	1.7	8-12*	43-44.9	47-65	42-60
This work	LMBA	0.2-2	10	9-15	43-45	51-72	44-62

TABLE I

COMPARISON WITH STATE-OF-THE-ART OF WIDEBAND LOAD-MODULATED PAS

^{*}Graphically estimated

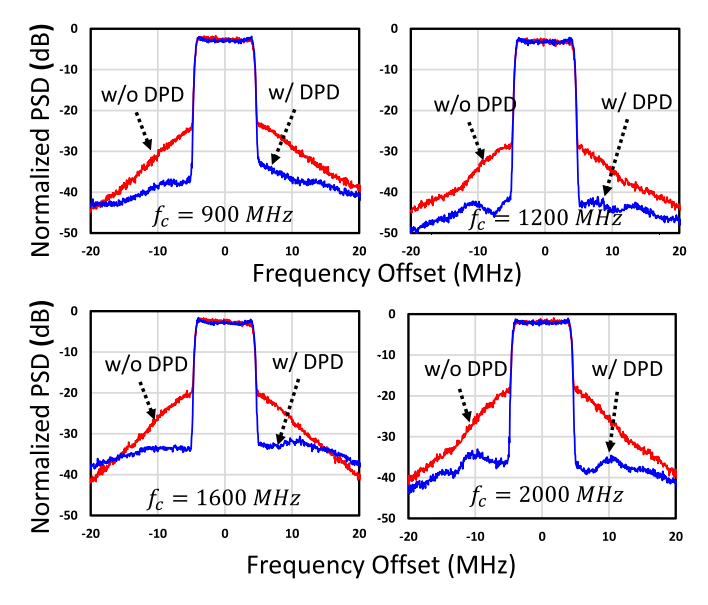


Fig. 24. Output spectrum with DPD.

to emphasize that the proposed PD-LMBA exhibits a decade bandwidth, the highest bandwidth among all reported loadmodulated PAs, while maintaining a highly competitive profile in terms of drain efficiency, back-off range, and gain.

B. Modulated Measurements

A 10-MHz-bandwidth 5G new radio (NR) signal with a PAPR of 10 dB is used to perform modulated measurements. The modulated signals are generated and analyzed using Keysight PXIe vector transceiver (VXT M9421). The average power of the modulated signals is around 32–34 dBm, and the output spectrum is shown in Fig. 23 at 200, 500, 900, 1200, 1600, and 2000 MHz, with average efficiency of 58%, 52%, 46%, 44%, 46%, and 45%, respectively. The measured adjacent channel leakage ratios (ACLR) at these frequencies are

below -21 dBc. After applying digital predistortion (DPD), the measured ACLR improves from -25.2 to -34.0 dBc at 0.9 GHz and from -21.2 to -34.1 dBc at 2.0 GHz, as shown in Fig. 24. The variations in DPD results at different frequencies are likely due to changes in the PA response across the entire bandwidth.

VI. CONCLUSION

This article presents a comprehensive analysis of LMBA from a signal-flow perspective. By constructing the full signal-flow graph of LMBA, it is, for the first time, demonstrated that the load modulation behavior of LMBA can be sustained across all in-band frequencies when a specific BA-CA phase-alignment condition is met. This finding not only provides a rigorous explanation of the wideband nature of LMBA but also introduces a novel design methodology for realizing LMBAs that fundamentally eliminates the bandwidth limitation imposed on practical LMBA design. Moreover, the signal-flow approach offers the opportunity to analyze the behavior of other load-modulated PA topologies from a new perspective. To prove the proposed concept, an ultrawideband RF-input PD-LMBA is designed and developed using GaN technology covering the frequency range from 0.2 to 2 GHz. The experimental results demonstrate an efficiency of 51%-72% for peak output power and 44%–62% for 10-dB OBO, respectively. By leveraging the BA-CA phase-alignment condition identified in this study, the bandwidth of the PD-LMBA prototype has been extended to an unprecedented decade-wide range, significantly outperforming the state-of-the-art.

ACKNOWLEDGMENT

The authors would like to thank Prof. Patrick Roblin of The Ohio State University for his insightful signal-flow graph of the BA from his lecture slides, and the signal-flow graph introduced in this article uses a similar drawing style. They also want to thank Ryan Baker of Wolfspeed (now MACOM) for providing transistor samples and Barry L. Johnson of Keysight Technologies for the technical support on DPD setup.

REFERENCES

- [1] Z. Popovic, "GaN power amplifiers with supply modulation," in *IEEE MTT-S Int. Microw. Symp. Dig.*, May 2015, pp. 1–4.
- [2] J. Kim et al., "Highly efficient RF transmitter over broad average power range using multilevel envelope-tracking power amplifier," *IEEE Trans. Circuits Syst. I, Reg. Papers*, vol. 62, no. 6, pp. 1648–1657, Jun. 2015.
- [3] C. M. Andersson, D. Gustafsson, J. C. Cahuana, R. Hellberg, and C. Fager, "A 1–3-GHz digitally controlled dual-RF input poweramplifier design based on a Doherty-outphasing continuum analysis," *IEEE Trans. Microw. Theory Techn.*, vol. 61, no. 10, pp. 3743–3752, Oct. 2013.
- [4] T. Barton, "Not just a phase: Outphasing power amplifiers," IEEE Microw. Mag., vol. 17, no. 2, pp. 18–31, Feb. 2016.
- [5] D. Mikrut, P. Roblin, C. Liang, S. Smith, and R. Tantawy, "Broadband outphasing power amplifier using Doherty-chireix continuum in a GaN MMIC process," in *Proc. IEEE Top. Conf. RF/Microw. Power Model. Radio Wireless Appl.*, Jan. 2023, pp. 13–15.
- [6] Y. Zheng and P. Roblin, "Bandwidth-enhanced mixed-mode outphasing power amplifiers based on the analytic role-exchange Doherty-chireix continuum theory," *IEEE Trans. Circuits Syst. I, Reg. Papers*, vol. 71, no. 8, pp. 3584–3596, Aug. 2024.
- [7] W. H. Doherty, "A new high efficiency power amplifier for modulated waves," *Proc. Inst. Radio Eng.*, vol. 24, no. 9, pp. 1163–1182, Sep. 1936.
- [8] G. Nikandish, R. B. Staszewski, and A. Zhu, "Breaking the bandwidth limit: A review of broadband Doherty power amplifier design for 5G," *IEEE Microw. Mag.*, vol. 21, no. 4, pp. 57–75, Apr. 2020.
- [9] M. Özen, K. Andersson, and C. Fager, "Symmetrical Doherty power amplifier with extended efficiency range," *IEEE Trans. Microw. Theory Techn.*, vol. 64, no. 4, pp. 1273–1284, Apr. 2016.
- [10] J. J. M. Rubio, V. Camarchia, M. Pirola, and R. Quaglia, "Design of an 87% fractional bandwidth Doherty power amplifier supported by a simplified bandwidth estimation method," *IEEE Trans. Microw. Theory Techn.*, vol. 66, no. 3, pp. 1319–1327, Mar. 2018.
- [11] Y. Xu, J. Pang, X. Wang, and A. Zhu, "Enhancing bandwidth and back-off range of Doherty power amplifier with modified load modulation network," *IEEE Trans. Microw. Theory Techn.*, vol. 69, no. 4, pp. 2291–2303, Apr. 2021.
- [12] H. Lyu and K. Chen, "Analysis and design of reconfigurable multiband mismatch-resilient quasi-balanced Doherty power amplifier for massive MIMO systems," *IEEE Trans. Microw. Theory Techn.*, vol. 70, no. 10, pp. 4410–4421, Oct. 2022.
- [13] H. Lyu, Y. Cao, and K. Chen, "Linearity-enhanced quasi-balanced Doherty power amplifier with mismatch resilience through series/parallel reconfiguration for massive MIMO," *IEEE Trans. Microw. Theory Techn.*, vol. 69, no. 4, pp. 2319–2335, Apr. 2021.
- [14] X. Zhang, S. Li, and T. Chi, "A millimeter-wave watt-level Doherty power amplifier in silicon," *IEEE Trans. Microw. Theory Techn.*, vol. 72, no. 3, pp. 1674–1686, Mar. 2024.
- [15] C. Liang, P. Roblin, Y. Hahn, J. I. Martinez-Lopez, H.-C. Chang, and V. Chen, "Single-input broadband hybrid Doherty power amplifiers design relying on a phase sliding-mode of the load modulation scheme," *IEEE Trans. Microw. Theory Techn.*, vol. 71, no. 4, pp. 1550–1562, Apr. 2023.
- [16] X. Fang, J. Shi, C. Wei, Y. Duan, P. Li, and Z. Wang, "A linear millimeter-wave GaN MMIC Doherty power amplifier with improved AM-AM and AM-PM characteristics," *IEEE Trans. Microw. Theory Techn.*, vol. 72, no. 8, pp. 4597–4610, Aug. 2024.
- [17] X.-H. Fang, H.-Y. Liu, K. M. Cheng, and S. Boumaiza, "Modified Doherty amplifier with extended bandwidth and back-off power range using optimized peak combining current ratio," *IEEE Trans. Microw. Theory Techn.*, vol. 66, no. 12, pp. 5347–5357, Dec. 2018.
- [18] J. Xia, W. Chen, F. Meng, C. Yu, and X. Zhu, "Improved three-stage Doherty amplifier design with impedance compensation in load combiner for broadband applications," *IEEE Trans. Microw. Theory Techn.*, vol. 67, no. 2, pp. 778–786, Feb. 2019.
- [19] D. J. Shepphard, J. Powell, and S. C. Cripps, "An efficient broadband reconfigurable power amplifier using active load modulation," *IEEE Microw. Wireless Compon. Lett.*, vol. 26, no. 6, pp. 443–445, Jun. 2016.

- [20] D. J. Shepphard, J. Powell, and S. C. Cripps, "A broadband reconfigurable load modulated balanced amplifier (LMBA)," in *IEEE MTT-S Int. Microw. Symp. Dig.*, Jun. 2017, pp. 947–949.
- [21] R. Quaglia and S. Cripps, "A load modulated balanced amplifier for telecom applications," *IEEE Trans. Microw. Theory Techn.*, vol. 66, no. 3, pp. 1328–1338, Mar. 2018.
- [22] P. H. Pednekar, E. Berry, and T. W. Barton, "RF-input load modulated balanced amplifier with octave bandwidth," *IEEE Trans. Microw. Theory Techn.*, vol. 65, no. 12, pp. 5181–5191, Dec. 2017.
- [23] P. H. Pednekar, W. Hallberg, C. Fager, and T. W. Barton, "Analysis and design of a Doherty-like RF-input load modulated balanced amplifier," *IEEE Trans. Microw. Theory Techn.*, vol. 66, no. 12, pp. 5322–5335, Dec. 2018.
- [24] Y. Cao and K. Chen, "Pseudo-Doherty load-modulated balanced amplifier with wide bandwidth and extended power back-off range," *IEEE Trans. Microw. Theory Techn.*, vol. 68, no. 7, pp. 3172–3183, Jul. 2020.
- [25] J. Pang et al., "Analysis and design of highly efficient wideband RF-input sequential load modulated balanced power amplifier," *IEEE Trans. Microw. Theory Techn.*, vol. 68, no. 5, pp. 1741–1753, May 2020.
- [26] Y. Cao, H. Lyu, and K. Chen, "Asymmetrical load modulated balanced amplifier with continuum of modulation ratio and dual-octave bandwidth," *IEEE Trans. Microw. Theory Techn.*, vol. 69, no. 1, pp. 682–696, Jan. 2021.
- [27] J. Guo, Y. Cao, and K. Chen, "1-D reconfigurable Pseudo-Doherty load modulated balanced amplifier with intrinsic VSWR resilience across wide bandwidth," *IEEE Trans. Microw. Theory Techn.*, vol. 71, no. 6, pp. 2465–2478, Jun. 2023.
- [28] C. Chu, J. Pang, R. Darraji, S. K. Dhar, T. Sharma, and A. Zhu, "Broad-band sequential load modulated balanced amplifier with extended design space using second harmonic manipulation," *IEEE Trans. Microw. Theory Techn.*, vol. 71, no. 5, pp. 1990–2003, May 2023.
- [29] C. Belchior, L. C. Nunes, P. M. Cabral, and J. C. Pedro, "Sequential LMBA design technique for improved bandwidth considering the balanced amplifiers off-state impedance," *IEEE Trans. Microw. Theory Techn.*, vol. 71, no. 8, pp. 3629–3643, Aug. 2023.
- [30] J. Pang, C. Chu, Y. Li, and A. Zhu, "Broadband RF-input continuous-mode load-modulated balanced power amplifier with input phase adjustment," *IEEE Trans. Microw. Theory Techn.*, vol. 68, no. 10, pp. 4466–4478, Oct. 2020.
- [31] J. Xie, K.-K.-M. Cheng, P. Yu, and X. Fang, "Dual-band pseudo-Doherty load modulated balanced amplifier design with arbitrarily selected frequency bands," *IEEE Trans. Circuits Syst. II, Exp. Briefs*, vol. 71, no. 8, pp. 3665–3669, Aug. 2024.
- [32] J. Xie, K.-K.-M. Cheng, X. Fang, and P. Yu, "Extension of output backoff range in three-stage load modulated balanced amplifier using asymmetric coupling and non-Z₀ load," *IEEE Trans. Microw. Theory Techn.*, early access, Jul. 18, 2024, doi: 10.1109/TMTT.2024.3425168.
- [33] N. B. Vangipurapu, P. Gong, J. Guo, and K. Chen, "Indirectly-Non-reciprocal load modulated balanced amplifier with equivalent operation at antenna interface," in *IEEE MTT-S Int. Microw. Symp. Dig.*, Jun. 2024, pp. 1032–1035.
- [34] Y. Cao, S. P. Gowri, N. B. Vangipurapu, and K. Chen, "High-power BAW-based FDD front-end using indirect-duplexing load modulated balanced amplifier for massive MIMO array," in *IEEE MTT-S Int. Microw. Symp. Dig.*, Jun. 2024, pp. 485–488.
- [35] N. B. Vangipurapu, H. Lyu, Y. Cao, and K. Chen, "Intrinsically mode-reconfigurable load-modulation power amplifier leveraging transistor's analog-digital duality," in *IEEE MTT-S Int. Microw. Symp. Dig.*, Jun. 2022, pp. 418–421.
- [36] J. Guo and K. Chen, "Load-modulated double-balanced amplifier with quasi-isolation to load," in *Proc. IEEE Wireless Microw. Technol. Conf.* (WAMICON), Apr. 2023, pp. 144–147.
- [37] H. Jia, R. Liu, Q. Wu, and A. Zhu, "A 26-GHz GaN MMIC load-modulated balanced amplifier with miniaturized dual-loop coupler," *IEEE Trans. Microw. Theory Techn.*, early access, Jul. 4, 2024, doi: 10.1109/TMTT.2024.3421941.
- [38] J. Guo, Y. Cao, and K. Chen, "Linear hybrid asymmetrical load-modulated balanced amplifier with multiband reconfigurability and antenna-vswr resilience," *IEEE Trans. Microw. Theory Techn.*, vol. 72, no. 9, pp. 5319–5332, Sep. 2024.
- [39] S. F. B. Faruquee, J. Guo, P. Gong, and K. Chen, "Hybrid load-modulated double-balanced amplifier (H-LMDBA) with four-way load modulation and >15-dB power back-off range," in *Proc. IEEE Wireless Microw. Technol. Conf. (WAMICON)*, Apr. 2024, pp. 1–4.

- [40] C. Chu et al., "Waveform engineered sequential load modulated balanced amplifier with continuous class-F1 and Class-J operation," *IEEE Trans. Microw. Theory Techn.*, vol. 70, no. 2, pp. 1269–1283, Feb. 2022.
- [41] P. Chen et al., "A theoretical method to optimize the control signal power for high-efficiency symmetrical load modulated balanced amplifier designs," *IEEE Microw. Wireless Technol. Lett.*, vol. 34, no. 2, pp. 211–214, Feb. 2024.
- [42] D. Regev, S. Shilo, D. Ezri, and G. Ming, "Modified re-configurable quadrature balanced power amplifiers for half and full duplex RF front ends," in *Proc. Texas Symp. Wireless Microw. Circuits Syst. (WMCS)*, Apr. 2018, pp. 1–4.
- [43] N. B. Vangipurapu and K. Chen, "Theory and design of quadrature-balanced GaN power amplifier as magnetic-less simultaneous transmit and receive (STAR) front-end," *IEEE Trans. Microw. Theory Techn.*, early access, Aug. 2, 2024, doi: 10.1109/TMTT.2024.3426474.
- [44] P. Gong, J. Guo, N. Bharadwaj Vangipurapu, and K. Chen, "Decade-bandwidth RF-input pseudo-Doherty load-modulated balanced amplifier using signal-flow-based phase alignment design," *IEEE Microw. Wireless Technol. Lett.*, vol. 34, no. 6, pp. 761–764, Jun. 2024.
- [45] S. C. Cripps, "RF power amplifiers for wireless communications," *IEEE Microw. Mag.*, vol. 1, no. 1, p. 64, Mar. 2000.
- [46] D. M. Pozar, Microwave Engineering, 3rd ed., Hoboken, NJ, USA: Wiley, 2005. [Online]. Available: https://cds.cern.ch/record/882338
- [47] X. Chen, W. Chen, F. M. Ghannouchi, and Z. Feng, "The nested-mode power amplifiers for highly efficient multi-octave applications," *IEEE Trans. Microw. Theory Techn.*, vol. 67, no. 12, pp. 5114–5126, Dec. 2019.
- [48] P. Gong, "Design of a broadband Doherty power amplifier with a graphical user interface tool," Master's thesis, Dept. Elect. Comput. Eng., Ohio State Univ., Columbusc, OH, USA, 2022. [Online]. Available: http://rave.ohiolink.edu/etdc/view?acc_num=osu1658158564568844
- [49] H. Jang, P. Roblin, and Z. Xie, "Model-based nonlinear embedding for power-amplifier design," *IEEE Trans. Microw. Theory Techn.*, vol. 62, no. 9, pp. 1986–2002, Sep. 2014.
- [50] P. J. Tasker and J. Benedikt, "Waveform inspired models and the harmonic balance emulator," *IEEE Microw. Mag.*, vol. 12, no. 2, pp. 38–54, Apr. 2011.
- [51] Y. Cao, H. Lyu, and K. Chen, "Continuous-mode hybrid asymmetrical load-modulated balanced amplifier with three-way modulation and multi-band reconfigurability," *IEEE Trans. Circuits Syst. I, Reg. Papers*, vol. 69, no. 3, pp. 1077–1090, Mar. 2022.



Pingzhu Gong (Student Member, IEEE) received the B.Eng. degree in electrical engineering from Tianjin University, Tianjin, China, in 2019, and the M.S. degree in electrical and computer engineering from The Ohio State University, Columbus, OH, USA, in 2022. He is currently pursuing the Ph.D. degree in electrical engineering at the University of Central Florida, Orlando, FL, USA.

His research interests include highly efficient and broadband power amplifier (PA) architectures in CMOS and GaN technologies.

Mr. Gong's paper was selected as a Finalist in the Best Student Paper Competition at IEEE MTT-S IMS 2024.



Jiachen Guo (Student Member, IEEE) received the M.S. degree in computer engineering from Syracuse University, Syracuse, NY, USA, in 2021. He is currently pursuing the Ph.D. degree in electrical engineering at the University of Central Florida, Orlando, FL, USA.

His research interests include novel, highly efficient broadband and linear power amplifier (PA) architectures and reconfigurable RF/millimeter-wave circuits design.

Mr. Guo was a recipient of the Second Place Award of the Student Design Competition on High Efficiency Power Amplifier at IEEE MTT-S IMS in 2020.



Niteesh Bharadwaj Vangipurapu (Graduate Student Member, IEEE) received the bachelor's degree in electronics and communication engineering from Visvesvaraya Technological University, Belgaum, India, in 2020, and the M.S. degree from the University of Central Florida, Orlando, FL, USA, in 2022, where he is currently pursuing the Ph.D. degree in electrical engineering.

His research interests include novel, highly efficient and linear power amplifier (PA) architectures. He is currently working on the design of

RF/mm-Wave circuits.

Mr. Vangipurapu was a recipient of the First Place Award of Student Paper Competition at IEEE WAMICON 2023. He currently serves as the Treasurer for the IEEE MTT-S/AP-S Orlando Chapter.



Kenle Chen (Senior Member, IEEE) received the bachelor's degree in communication engineering from Xi'an Jiaotong University, Xi'an, China, in 2005, the master's degree in electronics and information engineering from Peking University, Beijing, China, in 2008, and the Ph.D. degree in electrical engineering from Purdue University, West Lafayette, IN, USA, in 2013.

Prior to his career in academia, he has extensive experience in wireless and semiconductor industries. From 2013 to 2015, he was a Principal/Lead

RFIC Engineer with innovational startups, where he led the research and development of multiple successful products of CMOS integrated power amplifiers and front-end solutions for the latest WLAN platforms, e.g., IEEE802.11ac/ax. From 2015 to 2017, he was a Staff RFIC Engineer with Skyworks Solutions, Inc., Irvine, CA, USA, where he focused on the development of RF front-end modules for the advanced smartphone platforms. He is currently an Assistant Professor with the Department of Electrical and Computer Engineering, University of Central Florida, Orlando, FL, USA. His research interests include energy-efficient, wideband, and ultrahigh-speed RF/mm-Wave circuits and systems for 5G-and-beyond communications, extreme-performance power amplifiers in CMOS and compound semiconductor technologies, reconfigurable RF/mm-Wave electronics, and innovational wireless radio concepts/architectures/applications.

Dr. Chen was a recipient of the 2012 IEEE Microwave Theory and Techniques Society (MTT-S) Graduate Fellowship. He is an Associate Editor of IEEE TRANSACTIONS ON MICROWAVE THEORY AND TECHNIQUES.